CEνNS search with cryogenic sapphire detectors at MINER: Results from the TRIGA reactor data and future sensitivity at HFIR

D. Mondal,[1,2] W. Baker,[3] M. Chaudhuri,[1,2] J. B. Dent,[4] R. Dey,[1,2] B. Dutta,[3] V. Iyer,[5] A. Jastram,[6] V. K. S. Kashyap,[1,2] A. Kubik,[7] K. Lang,[8] R. Mahapatra,[3] S. Maludze,[3] N. Mirabolfathi,[3] M. Mirzakhani,[3] B. Mohanty,[1,2,*] H. Neog,[9] J. L. Newstead,[10] M. Platt,[3] S. Sahoo,[3] J. Sander,[11] L. E. Strigari,[3] and J. Walker[4]

(MINER Collaboration)

[1]*National Institute of Science Education and Research, Jatni-752050, Odisha, India*
[2]*Homi Bhabha National Institute, Training School Complex, Anushakti Nagar, Mumbai, 400094, Maharashtra, India*
[3]*Department of Physics and Astronomy, Texas A&M University, 578 University Drive, College Station, 77840, Texas, USA*
[4]*Department of Physics, Sam Houston State University, 1905 University Avenue, Huntsville, Texas, 77340, USA*
[5]*Department of Physics, University of Toronto, 27 King's College Circle, Toronto, Ontario, M5S 1A7, Canada*
[6]*Department of Mechanical Engineering, Texas A&M University, 202 Spence Street, College Station, 77840, Texas, USA*
[7]*SNOLAB, Creighton Mine No. 9, 1039 Regional Road 24, Sudbury, Ontario, P3Y 1N2, Canada*
[8]*Department of Physics, The University of Texas at Austin, 2515 Speedway, Austin, Texas, 78712, USA*
[9]*School of Physics and Astronomy, University of Minnesota, Minneapolis, Minnesota, 55455, USA*
[10]*ARC Centre of Excellence for Dark Matter Particle Physics, School of Physics, The University of Melbourne, Parkville, Victoria 3010, Australia*
[11]*Department of Physics, University of South Dakota, 414 East Clark Street, Vermillion, South Dakota, 57069, USA*

(Received 27 October 2025; accepted 13 July 2026; published 26 August 2026)

We report on a search for coherent elastic neutrino-nucleus scattering (CEνNS) using cryogenic sapphire (Al_2O_3) detectors deployed at the Mitchell Institute Neutrino Experiment at Reactor (MINER), located near the 1 MW_{th} TRIGA research reactor at Texas A&M University. The experiment operated with a primary detector mass of 72 g and achieved a baseline energy resolution of $\sim$40 eV. Using exposures of 158 g-days (reactor-ON) and 381 g-days (reactor-OFF), we performed a statistical background subtraction in the energy region of 0.25–3 keV. A Geant4 simulation has been performed to understand the reactor-correlated background present in the data, and it agrees with our observations. After accounting for this background, the profile-χ^2 analysis yields no statistically significant CEνNS excess. The best-fit signal strength is consistent with the physical boundary ($\rho = 0$), and we set a 90% confidence level upper limit of $\rho < 2213$ on the CEνNS rate relative to the Standard Model prediction. This result indicates that the current analysis is dominated by residual low-energy backgrounds. To have enhanced sensitivity, the MINER Collaboration plans to relocate the experiment to the 85 MW_{th} High Flux Isotope Reactor (HFIR) at Oak Ridge National Laboratory (ORNL). With improved shielding, increased detector mass, and higher antineutrino flux, the upgraded setup is projected to achieve a 3σ CEνNS detection within 30 kg-days of exposure.

DOI: 10.1103/115m-y8mg

I. INTRODUCTION

Neutrinos are among the most elusive particles in the Standard Model (SM), interacting only via the weak interaction. While processes such as inverse beta decay and neutrino-electron scattering have been widely used for neutrino detection, an alternative channel known as coherent elastic neutrino-nucleus scattering (CEνNS) offers a compelling probe of both SM and Beyond Standard Model physics.

CEνNS is a neutral-current process in which a neutrino scatters coherently off an entire nucleus:

*Contact author: bedanga@niser.ac.in

$$\nu + A(Z,N) \to \nu + A(Z,N). \quad (1)$$

This process becomes significant when the inverse momentum transfer is comparable to or larger than the nuclear radius, ensuring that the contributions from individual nucleons add coherently. Under these conditions, the CEνNS cross section is enhanced and approximately scales as the square of the neutron number, $\sigma \propto N^2$, making it a highly sensitive probe of weak interactions at low energies.

This neutral-current electroweak interaction was first predicted in 1974 [1] with a SM differential cross section [2]:

$$\frac{d\sigma}{dT}(E_\nu, T) = \frac{G_F^2 M}{4\pi}\left(1 - \frac{MT}{2E_\nu^2}\right)[F(Q^2)]^2 \mathcal{Q}_W^2, \quad (2)$$

where E_ν denotes the neutrino energy; T is the nuclear recoil energy; M is the target nucleus mass; G_F is the Fermi coupling constant; and $F(Q^2)$ represents the nuclear form factor, modeled using the Helm parametrization [3]; $Q^2 = -q^2$, q is the 4-momentum transfer to the target nucleus; and $\mathcal{Q}_W = N - (1 - 4\sin^2\theta_W)Z$ is the weak charge of the nucleus, considering only the tree-level values for the neutrino-to-proton $(g_V^p = \frac{1}{2} - 2\sin^2\theta_W)$ and neutron $(g_V^n = -\frac{1}{2})$ coupling parameters [3]. Having a small value of $\sin^2\theta_W \approx 0.23873 \pm 0.00005$ as mentioned by the Particle Data Group [4], the CEνNS interaction is predominantly sensitive to the number of neutrons inside the nucleus. Therefore, a detector material with a large atomic mass makes it a suitable choice for CEνNS search experiments. In contrast, a heavy nucleus produces very low recoil, making its detection very challenging.

Despite being predicted more than five decades ago, CEνNS was first observed only in 2017 by the COHERENT Collaboration using pion decay-at-rest neutrinos at the Spallation Neutron Source [5]. This milestone opened new avenues in neutrino physics, including the study of nonstandard neutrino interactions, precision measurements of the weak mixing angle [6], searches for light mediators [7], and investigations into neutrino electromagnetic properties such as magnetic moment [6,8] and charge radius [9]. Beyond its role in constraining new physics, CEνNS offers a unique tool for studying the nuclear structure itself. Since the CEνNS cross section is primarily sensitive to the weak charge of the nucleus, which is dominated by neutrons, precise CEνNS measurements can provide access to the neutron distribution and form factor [10].

Nuclear reactors are ideal sources of low-energy (up to $\sim$10 MeV) antineutrinos, fully within the coherent scattering regime. Unlike accelerator sources, reactor-based CEνNS searches benefit from a continuous and intense flux of $\bar{\nu}_e$ with average energies well suited for maximal coherence [11]. Furthermore, reactor antineutrino detection through CEνNS can serve as a powerful tool for reactor monitoring [12], nuclear safeguards, and understanding the irreducible neutrino background often referred to as the "neutrino floor" in direct dark matter searches [13].

Several reactor-based CEνNS experiments are currently operational or under development, including CONUS+ [14], TEXONO [15], CONNIE [16], NUCLEUS [17], Ricochet [18,19], and νGEN [20]. In this context, the Mitchell Institute Neutrino Experiment at Reactor (MINER) deploys low-threshold cryogenic sapphire detectors at close proximity to a reactor core. In addition to CEνNS searches, the same experimental setup has recently been employed to search for axion-like particles, demonstrating the broader physics reach of the MINER [21,22].

This paper presents the results of CEνNS search using data collected at MINER during its operation at the Texas A&M University TRIGA reactor. We describe the experimental setup, detector response, event selection, and statistical treatment of the data. We also outline the prospects for significantly improved sensitivity in the upcoming MINER at HFIR deployment at the High Flux Isotope Reactor (HFIR) at Oak Ridge National Laboratory.

II. MINER EXPERIMENT

A. Reactor

The Mitchell Institute Neutrino Experiment at Reactor (MINER) is a reactor-based CEνNS experiment located at the Nuclear Science Center (NSC) at Texas A&M University. It utilizes a research reactor, called TRIGA (Training, Research, Isotope production, General Atomics), with an optimal power of 1 $\mathrm{MW_{th}}$ fueled with low-enriched uranium (LEU, 20% ^{235}U). This reactor produces a high flux of antineutrinos ($\bar{\nu}_e$) via beta decay of fission fragments. At a baseline of $\sim$4 m from the core, the $\bar{\nu}_e$ flux is approximately $10^{10}\ \mathrm{cm^{-2}\,s^{-1}}$, estimated using the method described in Ref. [23].

B. Detector concept and cryogenic setup

MINER employs cryogenic sapphire detectors to achieve the low recoil threshold required for CEνNS detection [24]. The detectors operate at $\mathcal{O}(10\ \mathrm{mK})$, enabling phonon-based readout with excellent energy resolution and minimal thermal noise. Cooling is provided by a BlueFors dilution refrigerator with a base temperature of approximately 10 mK.

During the data collection period, a tower of three sapphire detectors was installed inside the dilution refrigerator, which had a 4 mm–thick primary detector [25] sandwiched between two 10 mm–thick top and bottom active veto detectors. These veto detectors are used to reject backgrounds. Each crystal features photolithographically patterned phonon sensors on its top surface, known as quasiparticle-assisted electrothermal feedback transition-edge sensors (QETs) [26]. These sensors detect athermal phonons produced during particle interactions. As phonons are absorbed, the transition edge sensor (TES) transitions

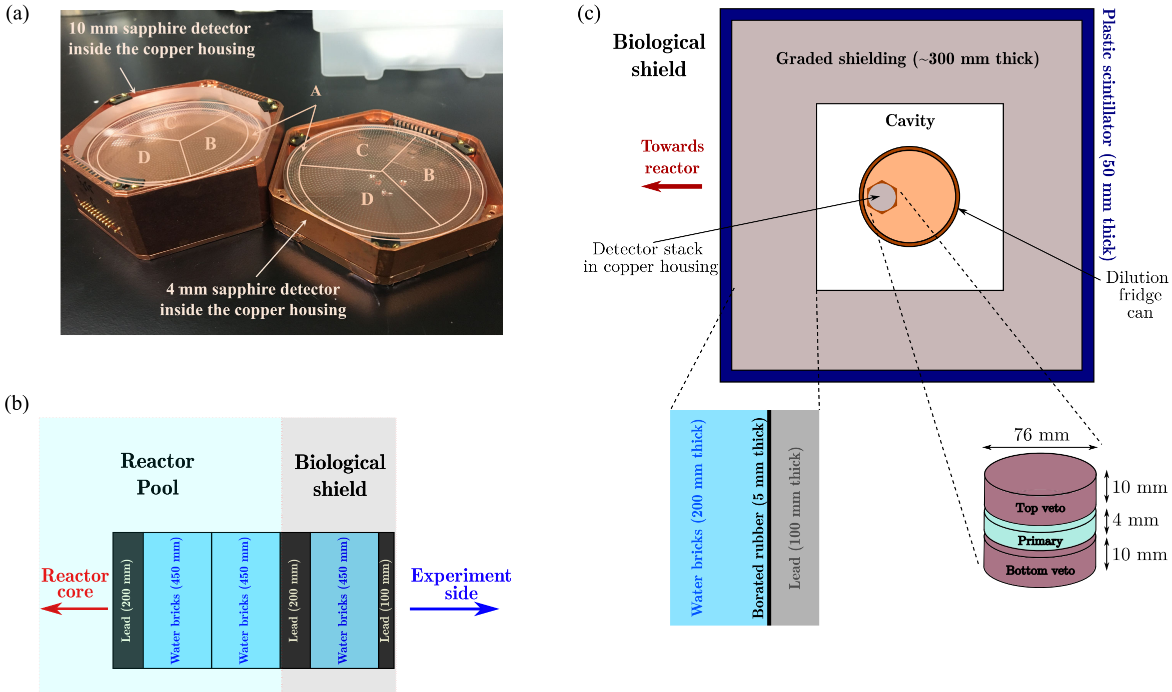

FIG. 1. (a) Photograph of the primary (4 mm) and veto (10 mm) sapphire detector with the phonon sensors photolithographically patterned on the surface. (b) Schematic of the cavity packed with layered shielding. (c) Detector shielding (top view) showing the placement of the detector stack inside the dilution fridge.

from superconducting to normal state, inducing a signal that is read out via a SQUID-based circuit [27]. Each of the detectors is cylindrical, with four phonon channels: one outer annular channel A and three bulk channels B, C, and D, as shown in Fig. 1(a). The detectors were operated without a bias voltage. The specifications of the detectors are listed in Table I.

C. Shielding and experimental configuration

The biological shield surrounding the reactor pool in the NSC facility is made of ~2 m–thick high-density concrete (~3.5 g/cm^3 density). It comprises a cavity inside it to facilitate near-reactor experiments as described in Ref. [28]. During the measurement period, the cavity was filled with layers of water and lead to stop gamma and neutrons produced inside the reactor core from reaching the experimental area. The cavity from the reactor core to the biological shield toward the experimental side was packed with layers of 200 mm–thick lead, two 450 mm–thick water brick layers, a 200 mm–thick lead layer, a 450 mm–thick water brick layer, and finally 100 mm–thick lead, as shown in Fig. 1(b). In addition to these, multilayered shielding was also constructed around the dilution refrigerator containing detectors to suppress environmental and reactor backgrounds, as shown in Fig. 1(c). From inside to outside, the detector shielding included a 100 mm–thick layer of lead, lined with a 5 mm–thick layer of borated (52%) rubber, a 200 mm–thick water brick layer, and a 50 mm–thick active muon veto made from a plastic scintillator. Water bricks were used to thermalize the neutrons, and borated rubber was used to capture the thermal neutrons. Additionally, the innermost lead layer stops the high-energy ambient gamma, as well as the gamma produced from the neutron capture in the borated rubber layer. The muon veto was not used for background rejection, as the low-energy excess background observed in Fig. 10, which increases exponentially, could not be reduced by applying an anti-coincidence cut with the muon scintillator panels.

TABLE I. Specifications of the sapphire detectors used in the MINER tower.

Detector parameter	Top veto	Primary (signal)	Bottom veto
Material	Al_2O_3	Al_2O_3	Al_2O_3
Diameter (mm)	76	76	76
Thickness (mm)	10	4	10
Density (g/cm^3)	3.98	3.98	3.98
Mass (g)	180	72	180

D. Data acquisition system

The energy depositions and the event timestamps of each detector channel are digitized using a VME-based CAEN V1740D multichannel ADC. It offers 64 input channels, 12-bit resolution, and a sampling rate of 62.5 MS/s. A 12-bit resolution over a ±1 V input range corresponds to a least significant bit (LSB) of approximately 0.5 mV, which is suitable for the expected noise from the readout system. Typical pulse amplitudes range from a few millivolts up to several hundred millivolts depending on the deposited energy. Instead of hardware triggering, a software-based triggering algorithm (SWT) [29] was employed to extract events from continuous voltage traces, enabling high-efficiency pulse selection in the low-energy regime.

III. MEASUREMENT

A. Data collection and overview

The analysis presented in this work is based on data collected at MINER during August–September 2022. This includes both reactor-ON and reactor-OFF conditions, with exposures of 158 and 381 g-days, respectively. The reactor was operating in this duration with a power of ~ 1 MW_{th}. The datasets were segmented into subruns, each processed and calibrated independently before being combined for the final analysis. The reactor-OFF data were used to benchmark the background, capturing contributions from environmental radioactivity and cosmic rays. A statistical subtraction method is employed to eliminate the reactor-OFF background from the reactor-ON data. Reactor-ON data were primarily collected during reactor operating hours, whereas reactor-OFF data were collected during reactor shutdown periods. Detector calibration, baseline resolution, and event selection were independently monitored for all data-taking periods, and no statistically significant time-dependent variations were observed.

B. Event reconstruction and pulse selection

Continuous voltage traces from each detector channel were recorded in the data acquisition system and processed using the SWT to extract individual pulse events, each approximately 2 ms long. The extracted traces were further processed using the Optimal Filter (OF) algorithm [30,31] to extract the energy information. The OF algorithm estimates the pulse amplitude, enhancing the signal-to-noise ratio by performing a frequency domain fit between the observed pulse and a reference template. This template is generated from the average of triggered signals, whereas the noise power spectral density (PSD) is derived from randomly triggered traces. The OF output amplitude from each of the four channels of any of the detectors is summed to produce a total amplitude, which is proportional to the energy deposited in that detector.

A representative pulse template [Fig. 2(a)], noise PSD [Fig. 2(b)], and a typical triggered phonon pulse [Fig. 2(c)] illustrate the components of the OF input. Figure 2(d) shows the resulting uncalibrated energy spectrum of the primary detector after summing up the OF amplitude of the four channels. The broad peak-like structures observed at higher amplitude in Fig. 2(d) correspond to high-energy

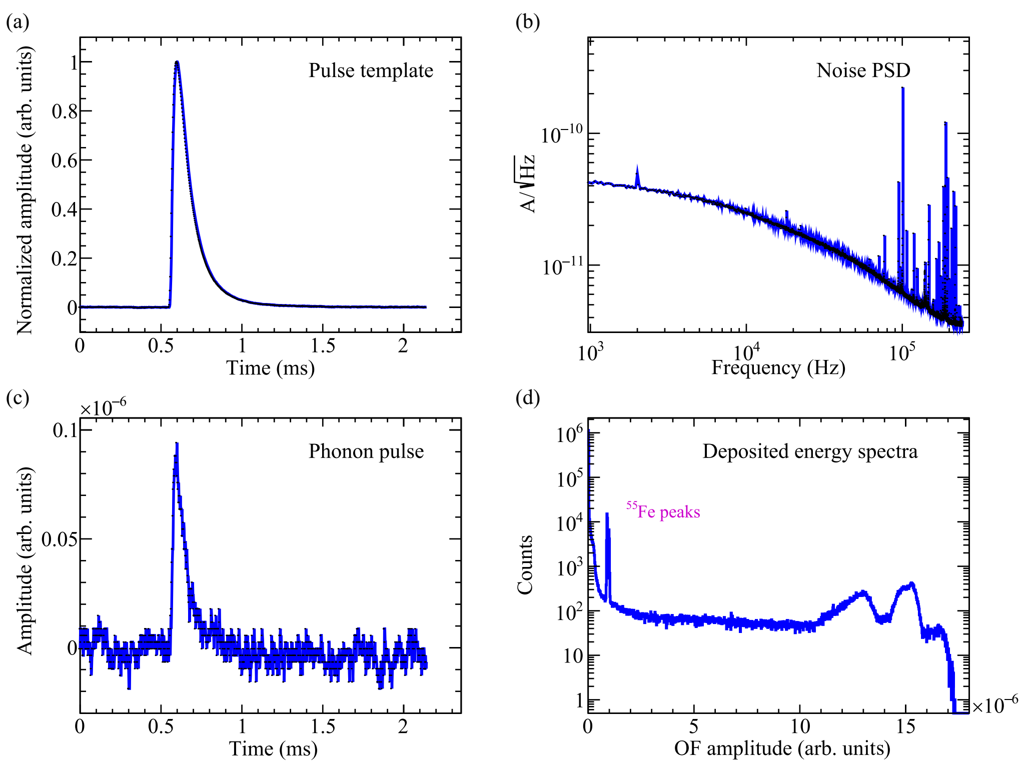

FIG. 2. (a) A representative phonon pulse template, (b) noise performance of the detector quantified in terms of the noise power spectral density (PSD), (c) a 590 eV phonon pulse before calibration, and (d) the uncalibrated energy spectrum observed in the primary detector.

deposition in the detector, which leads to the TES saturation and incomplete estimation of the energy deposition. There are also some pileup events and electronic glitches, which result in some bad pulses with large χ^2 values. Events with poor fits (large χ^2) are rejected to eliminate saturated, pileup, and instrumental artifacts.

C. Energy calibration

The calibration of the three detectors was performed using two ^{55}Fe sources. One source was placed between the top veto and the primary detector, and the second one was kept below the bottom veto detector, aligned with the central axis of the detector tower. These sources emit characteristic x-rays at 5.89 keV (K_α) and 6.49 keV (K_β) [32], which appear as well-resolved peaks in the response of the signal detector (Fig. 3). The OF amplitude (sum of four channels) spectrum of each detector was calibrated by fitting the peaks with a double Gaussian and establishing a linear relationship between known energies and measured amplitudes. These calibration functions are then used to convert OF amplitudes in the full dataset into energy units (keV). Since data taking was conducted in multiple periods rather than continuously, the calibration procedure was repeated for different data-taking intervals and for both reactor-ON and -OFF conditions. Figure 5 shows that the normalized calibration factor of the primary detector remains consistent throughout the data-taking campaign, indicating stable detector response and no significant variation between reactor-ON and -OFF periods. The calibrated and normalized energy spectra of the ON and OFF periods of the reactor are shown in Fig. 4.

The baseline energy resolution, denoted by σ, is defined as the standard deviation of the energy spectrum of randomly triggered noise traces. It quantifies the intrinsic noise of the detector and determines the minimum detectable energy. The range of resolutions across different sub-datasets for three detectors is listed in Table II. The resolutions provided here correspond to the summed resolution of all four channels in the detector. For the primary detector, the observed ~12% variation in baseline resolution across different data-taking periods has been incorporated into the systematic uncertainty associated with the threshold selection. Our achieved per-channel resolution is 28 eV [25], which corresponds to a sub-100 eV threshold for low-energy events if the primary channel is used for energy estimates. Figure 5 shows that the baseline resolution of the primary detector remained stable throughout the data-taking campaign, exhibiting only modest variations over time.

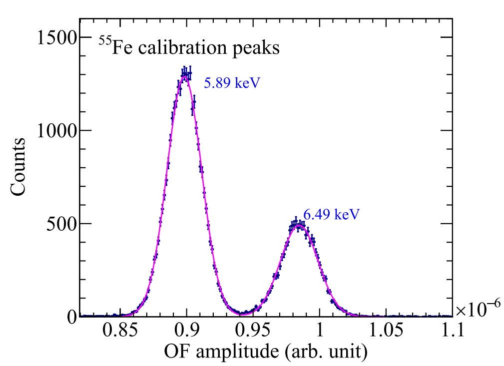

FIG. 3. X-ray peaks at 5.89 and 6.49 keV from the ^{55}Fe calibration source as observed in the primary detector. The double Gaussian fit function is shown in magenta to extract the mean positions.

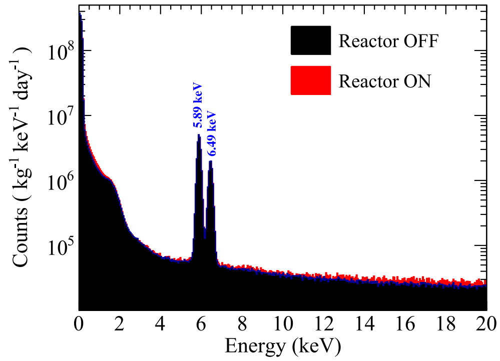

FIG. 4. Energy spectra of events collected during 158 g-days (reactor-ON) and 381 g-days (reactor-OFF) within the 0–20 keV energy range. The two prominent peaks correspond to the 5.89 and 6.49 keV x-rays from the ^{55}Fe calibration source.

D. Signal selection and background rejection

Due to the low CEνNS cross section ($< 10^{-40}$ cm^2), genuine signal events are expected to deposit energy only in the primary detector. This motivates the selection of only single-scatter events [Fig. 6(a)], where the primary detector must register an energy deposition above the threshold ($> 3\sigma$), while the top and bottom veto detectors remain within their noise levels ($< 2\sigma$), defined by their baseline resolutions for each run. Additionally, the four phonon channels (A, B, C, D) in the primary detector must trigger within a 0.2 ms window [Fig. 6(c)], ensuring that the signal originates from a single correlated interaction.

Moreover, surface events, which predominantly arise from background interactions, can mimic low-energy bulk events when a large fraction of the deposited energy is collected in the outer channel (channel A). These are identified using the A/sum parameter, which is the ratio of the OF amplitude in channel A to the sum of the OF amplitudes of all four channels. A selection cut is applied to select events with a disproportionately low outer-channel

TABLE II. Baseline energy resolution (1σ) for the three detectors across all sub-datasets.

Detector	Baseline resolution (eV)
Top veto	107–125
Primary (signal)	40–45
Bottom veto	110–142

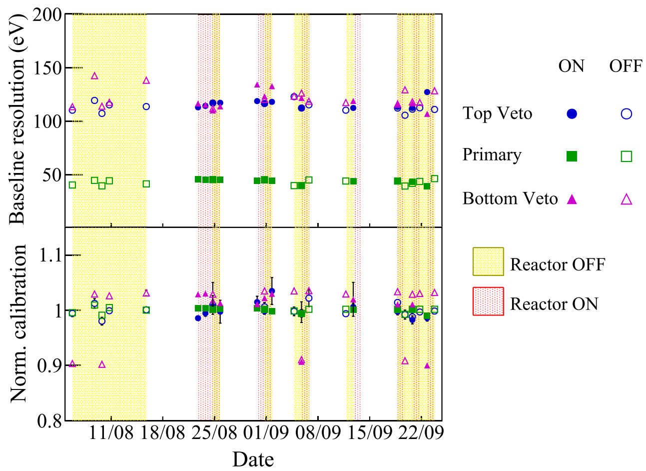

FIG. 5. Baseline and calibration (normalized) stability of the three detectors (top veto, primary detector, and bottom veto) over the duration of the run, including both reactor-OFF (yellow shaded region) and reactor-ON (red shaded region) periods.

contribution, thereby suppressing surface-event contamination in the bulk event sample.

After all cuts, the differential event rate spectra for reactor-ON and reactor-OFF periods are shown in Fig. 7 (top panel). The residual spectrum obtained by subtracting reactor-OFF from reactor-ON is shown in the bottom panel. This residual includes contributions from potential CEνNS events and additional reactor-induced gamma and neutron backgrounds. An inset in the bottom panel highlights the signal-like event rate in the low-energy region from 250 eV to 3 keV. As an additional stability check, the ON-OFF residual was evaluated in a signal-free sideband region. The residual rate was found to be consistent with zero within statistical uncertainties, supporting the stability of the subtraction procedure.

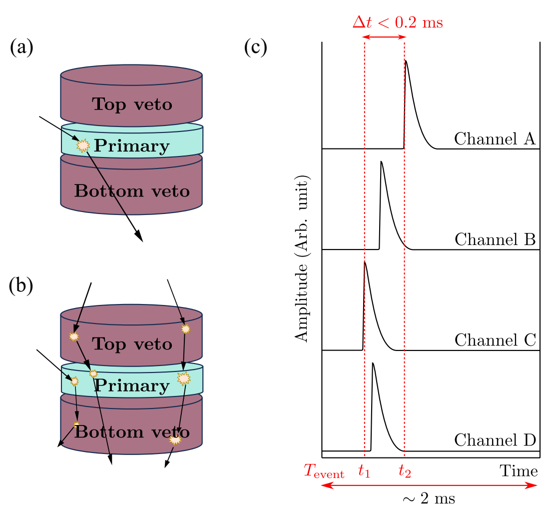

FIG. 6. Schematic illustration of (a) a single-scatter (signal-like), (b) a multiple-scatter (background-like) event within the detector stack, and (c) the time coincidence definition of the primary detector.

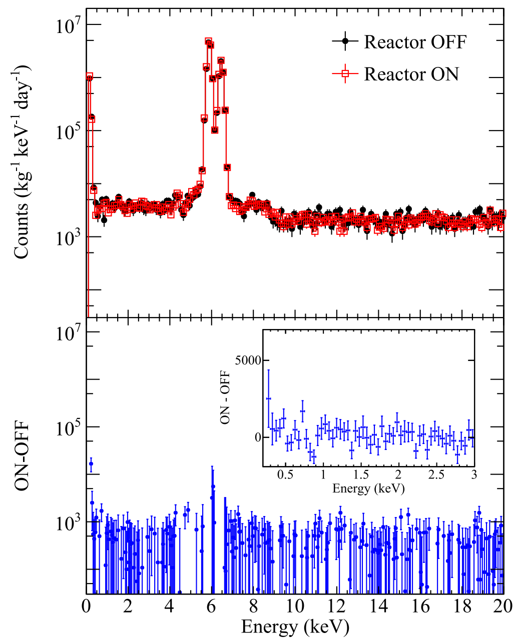

FIG. 7. Top panel: event rate after applying the single-scatter and fiducial-volume cuts, shown per keV per kg per day in the 0–20 keV energy range, before efficiency correction. The two prominent peaks correspond to the x-ray lines from the ^{55}Fe calibration source. Bottom panel: residual spectrum of signal-like events obtained by subtracting the reactor-OFF spectrum from the reactor-ON spectrum. An inset shows a zoomed-in view of the residual spectrum in the region of interest from 250 eV to 3 keV.

E. Efficiency correction and estimation of systematic uncertainties

The application of various selection criteria, such as event trigger, χ^2 cuts, single-scatter selection, and fiducialization, can result in the loss of genuine signal-like events, especially at low recoil energies. To estimate this, a Monte Carlo simulation was performed in which artificial signal pulses were generated by injecting the average pulse template into random noise traces. The simulated dataset was binned in energy (0–3 keV range, 50 eV bins), with 100 fake events per bin. These were subjected to the same data processing and selection criteria as the real data. To quantify event selection efficiency, we also compute the passage fraction, defined as the fraction of simulated events retained after each cut, and the result is presented in Table III for both reactor-ON and -OFF datasets. The largest relative difference between the reactor-ON and -OFF passage fractions is less than 0.4%, while the dominant uncertainty in the final measurement is found to be statistical. This indicates that the selection procedure is stable between the two reactor states and does not introduce a significant systematic bias in the present analysis.

The resulting energy-dependent efficiency is defined as the fraction of accepted events in each bin and is fitted using a sigmoid-plus-constant function, as shown in Fig. 8. This function is later used to correct both the ON and OFF measured event rate spectra. As shown in the inset of Fig. 8,

TABLE III. Typical passage fractions of signal-like events after each selection cut is applied separately.

Cut applied	Passage fraction (%)	
	OFF	ON
χ^2 quality cut	99.90	99.97
Single-scatter requirement	90.36	90.02
Fiducial-volume cut (A/sum)	90.65	90.65
Average	93.64	93.55

the efficiency curves for the reactor-ON and -OFF samples overlap within their statistical uncertainties across the full energy range considered. This demonstrates that the detector response and event-selection efficiencies are consistent between the two datasets and supports the use of a common efficiency correction.

In our analysis, the energy threshold is set at approximately 5.5σ, corresponding to about 250 eV, where σ denotes the baseline energy resolution of the primary detector. From the fitted efficiency function, modeled as a sigmoid plus a constant term, we obtain a 50% turn-on point at (0.245 ± 0.017) keV, which is consistent with the chosen analysis threshold of 250 eV.

The systematic uncertainties arising from the application of various analysis cuts were evaluated by varying selection thresholds and reanalyzing the datasets. The resulting uncertainties are propagated and summarized in Table IV. Although the single-scatter selection cut is the dominant systematic uncertainty (6.77%) in this analysis, the statistical uncertainty from the measurement is much higher than the combined systematics. The experimentally measured integrated signal plus the background rate after incorporating the statistical and systematic uncertainties is $R_{\mathrm{S+B}} \approx 341 \pm 229\,(\mathrm{stat}) \pm 23\,(\mathrm{sys})\ \mathrm{kg}^{-1}\,\mathrm{day}^{-1}$.

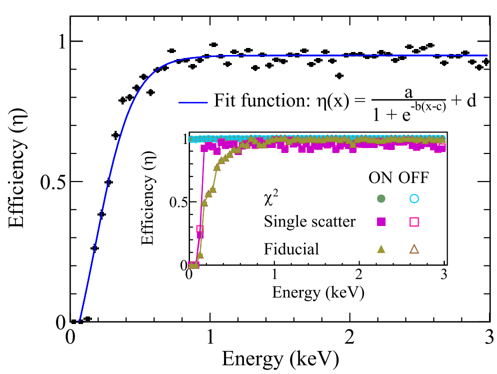

FIG. 8. Signal efficiency as a function of energy obtained from the combined application of the trigger requirement, χ^2 cut, single-scatter selection, and fiducial-volume cut. The fitted sigmoid-plus-constant function is shown in blue, and the component-wise efficiency for both reactor-ON and -OFF is shown in an inset.

TABLE IV. Systematics of combined reactor-ON and -OFF spectra related to different analysis cuts.

Analysis cut	Systematic (%)
χ^2 quality cut	0.055
Single-scatter	6.76
Fiducial-volume cut (A/sum)	0.27
All combined	6.77

F. Geant4-based reactor-ON background simulation

The complete experimental setup described in Sec. II C is modeled using the Geant4 (v11.2.1) [33] Monte Carlo framework, as shown in Fig. 9. The motivation is to benchmark the experimental findings. Since this analysis is based on the statistical subtraction method, the on-minus-off reactor spectrum consists primarily of the CEνNS signal together with background contributions. Although small residual effects from cosmic and environmental sources may persist, the dominant background is anticipated to originate from reactor-induced gammas and neutrons, particularly fast neutrons.

The "shielding" physics list is used to incorporate standard neutron and gamma interactions with matter. To reduce computational time and obtain good statistics, the simulated geometry is divided into two steps. In the first step, the reactor gammas and fast neutrons ($>$ 100 keV) are generated using the MCNP energy spectra presented in Ref. [28] from a plane $30 \times 30\ \mathrm{cm}^2$ facing the experimental site from the reactor. The kinetic energy and direction of the particles reaching the end of the biological shielding are recorded. In the second step, particles (gamma and neutrons) are sampled from the recorded information and propagated toward the experimental shielding, and eventually to the detector setup. An energy-dependent resolution, adapted from Ref. [34], is folded with the simulation.

In Fig. 10, the single-scatter event spectrum obtained after subtracting the reactor-OFF data from the reactor-ON data and efficiency correction is compared with the simulated reactor-correlated background spectrum for single-scattering events. The figure also shows that the reactor-correlated background is predominantly neutron-induced. The simulated spectrum exhibits reasonable agreement with the experimental data over most of the energy range, except at low energies. The origin of this low-energy discrepancy is presently under investigation and may arise from detector-related backgrounds not included in the current simulation [35–38] and observed by many low-threshold experiments. Overall, the simulation indicates that the experimentally observed spectrum is dominated by reactor-induced backgrounds, with event rates of the same order of magnitude as those measured in the data.

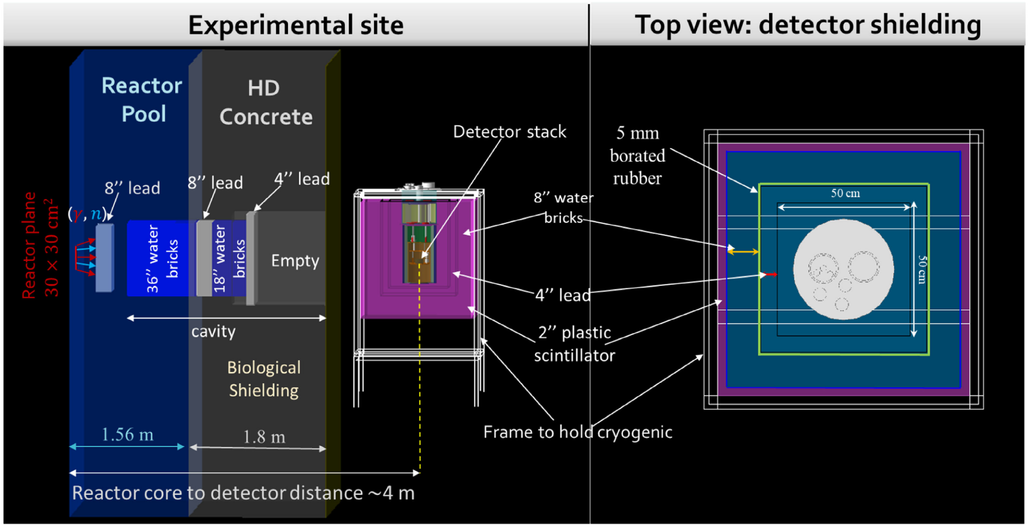

FIG. 9. Geant4-based geometry model of the experimental site (side view) and the simulated composite shielding around the dilution refrigerator (top view). Different shielding materials are shown in different colors: lead (light gray), water (blue), plastic scintillator (violet), and 52% borated rubber (green).

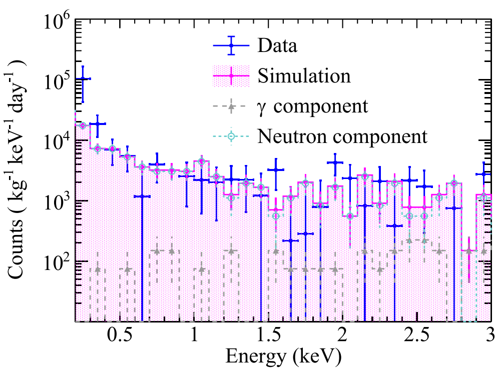

FIG. 10. Comparison of the simulated single-scatter spectra from neutron and gamma backgrounds, estimated using the Geant4 simulation and the shielding configuration shown in Fig. 9, with the measured single-scatter spectrum in the primary detector after subtraction of the reactor-OFF events. The green and gray spectra indicate the neutron- and gamma-induced background components, respectively, contributing to the total simulated spectrum.

IV. RESULTS AND DISCUSSION

A. Signal modeling

A signal model based on the SM prediction has been developed to estimate the expected CEνNS event rates in the current experimental configuration. The model uses the input parameters listed in Table V and follows the formalism described in Ref. [23]. The simulated differential electron antineutrino flux at the detector location, located ~4 m from the reactor, is shown in Fig. 11(a) as a function of neutrino energy. We have considered the contributions from the beta decay of four major fissioning isotopes: ^{235}U, ^{238}U, ^{239}Pu, ^{241}Pu. The neutron capture in ^{238}U produces $\bar{\nu}_e$ of energy < 1.3 MeV (16% of the total flux) [39]. These low-energy neutrinos are not relevant to our analysis, as only neutrinos with energy > 1.36 MeV will contribute to the signal in our region of interest. The antineutrino spectrum above 2 MeV is well studied, with an uncertainty of 5%, whereas the spectrum below is less understood. We have considered a conservative uncertainty of 30% [40] for the neutrino flux below 2 MeV. The $\bar{\nu}_e$ from the reactor having an energy greater than ~1.36 MeV introduce an overall 16% systematic uncertainty in the rate above the analysis threshold.

The corresponding CEνNS event rate spectra expected from individual interactions with aluminium and oxygen nuclei in the Al_2O_3 (sapphire) target are shown in Fig. 11(b). The cyan-shaded band indicates the region of interest (ROI), defined from 0.25 to 3 keV nuclear recoil energy. The upper bound of 3 keV is chosen, since the predicted signal rate drops below 10^{-2} kg^{-1} keV^{-1} day^{-1} beyond this point, rendering the signal statistically insignificant.

TABLE V. Parameters used for calculating the expected SM CEνNS signal.

Parameters	Values
Reactor power	~1 MW$_{th}$
Average fission fraction [41]	^{235}U (96.7%), ^{239}Pu (2%), ^{238}U (1.3%), ^{241}Pu (< 0.1%)
Baseline distance (d)	~4 m
Duty cycle (d_c)	100%
Target material	Al_2O_3
Detector efficiency (ϵ)	100%
Detector threshold	250 eV
Detector mass (m)	72 g

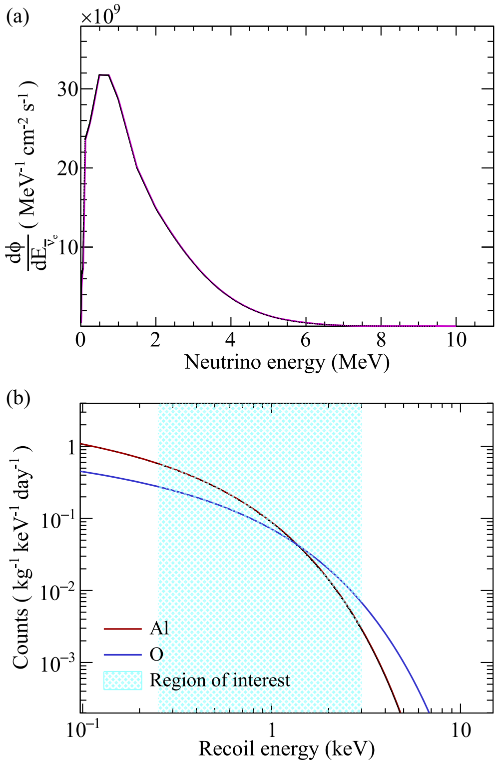

FIG. 11. (a) Simulated $\bar{\nu}_e$ flux from the reactor (approximately, 1 MW_{th}) incident on the detector located approximately 4 m away from the core. (b) Expected CEνNS event rate spectra for interactions with Al and O nuclei in sapphire. The cyan-shaded region indicates the analysis region of interest (ROI) [0.25–3] keV.

For further statistical analysis, the signal rate is calculated as a weighted average of the spectra from both the aluminium and oxygen nuclei in differential rate units (DRU, per kg per keV per day), accounting for their stoichiometric ratios in the sapphire target.

B. Statistical analysis

A χ^2 minimization analysis is performed in the region of interest (ROI), which spans 0.25–3 keV, with an energy-bin width of 50 eV. The test statistic is defined in Eq. (3) (adopted from Refs. [42,43]):

$$\chi^2(\delta,\beta,\zeta;\rho) = \sum_i \left[\frac{[R_i^{\mathrm{ON}} - \rho(1+\delta)R_i^{\mathrm{SM}} - (1+\beta)R_i^{\mathrm{sim}} - (1+\zeta)R_i^{\mathrm{OFF}}]^2}{\sigma_{i,\mathrm{ON}}^2 + (1+\zeta)^2\sigma_{i,\mathrm{OFF}}^2}\right] + \sum_{k=\delta,\beta,\zeta}\left(\frac{k}{\sigma_k}\right)^2. \tag{3}$$

Here, R_i^{ON} denotes the measured, efficiency-corrected reactor-ON event rate, and R_i^{OFF} denotes the reactor-OFF event rate in the ith energy bin. The quantities R_i^{SM} and R_i^{sim} represent the theoretical event rate estimated from the signal modeling and the background spectrum obtained from the Geant4 simulation, respectively. The terms $\sigma_{i,\mathrm{ON}}$ and $\sigma_{i,\mathrm{OFF}}$ correspond to the statistical uncertainties of the reactor-ON and reactor-OFF spectra in the ith bin. The parameter ρ is a scaling factor representing the ratio of the measured to the predicted cross section. The χ^2 is minimized with respect to the pull parameters δ, β, and ζ, incorporating systematic uncertainties of 16% (σ_δ), 10% (σ_β), and 6.77% (σ_ζ), respectively. The systematic uncertainty associated with signal modeling (σ_δ) is discussed in Sec. IV A. A conservative systematic uncertainty is assigned to the simulation (σ_β), while $\sigma_\zeta = 6.77\%$ corresponds to the uncertainty in the reactor-OFF spectrum derived from data. The 90% confidence limit is extracted using a χ^2 test statistic.

Since modeling the phonon response of the detector to the deposited energy is quite complex, the correction for fiducial volume in the Geant4 prediction was performed by scaling the single-scatter spectrum by the ratio of events remaining after the fiducial-volume cut to those after the single-scatter cut, based on data. Given the good agreement between the measured and simulated single-scatter spectra, this approach provides a reasonable estimate of the fiducialized event rate in the absence of a full phonon-transport simulation. Figure 12(a) shows the efficiency-corrected ON-OFF residual spectrum after subtraction of the simulated reactor-correlated background within the ROI. The spectrum is overlaid with the Standard Model CEνNS prediction scaled to the 90% CL upper limit obtained from the profile-χ^2 analysis. The fit is performed with the physical constraint $\rho \geq 0$, and the best-fit value is therefore found at the boundary ($\rho \simeq 0$), indicating no evidence for a CEνNS signal. The corresponding 90% CL upper limit is $\rho < 2213$, derived from the profile-χ^2 criterion $\Delta\chi^2 = 2.71$ (see Appendix A). The increase in uncertainty near the 250 eV threshold reflects the reduced detection efficiency at the lowest recoil energies.

Based on the SM prediction, the expected CEνNS event rate (R_{S}) in the ROI during the reactor-ON period is approximately 0.14 $\mathrm{kg}^{-1}\,\mathrm{day}^{-1}$. In contrast, the experimentally measured integrated rate is $R_{\mathrm{S+B}} \approx 341 \pm 229\,(\mathrm{stat}) \pm 23\,(\mathrm{sys})\ \mathrm{kg}^{-1}\,\mathrm{day}^{-1}$, whereas the event rate after accounting for reactor-correlated backgrounds using a simulation-informed model is $59 \pm 363\,(\mathrm{stat}) \pm 4\,(\mathrm{sys})\ \mathrm{kg}^{-1}\,\mathrm{day}^{-1}$. The significance of the observed signal is quantified as

$$\alpha = \frac{N_{\mathrm{S}}}{\sqrt{N_{\mathrm{S+B}}}}, \tag{4}$$

where N_{S} and $N_{\mathrm{S+B}}$ are the total predicted signal and observed signal plus background events, respectively, obtained by multiplying the corresponding rates with the reactor-ON exposure. The resulting significance is $\alpha = 0.01\sigma$.

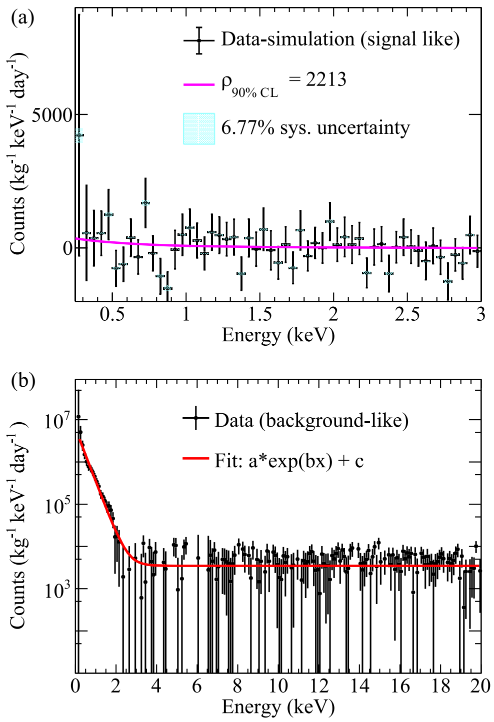

FIG. 12. (a) Efficiency-corrected reactor–ON-OFF signal spectrum after subtracting modeled reactor-ON backgrounds with associated uncertainties in the 250 eV to 3 keV energy range. The magenta lines represent the 90% confidence level (CL) upper-limit models. The cyan band indicates the systematic uncertainty. (b) Efficiency-corrected reactor–ON-OFF background spectrum (multiple scatter events), fitted with an exponential-plus-constant model.

The observed enhancement in the single-scatter event rate, at the level of $\mathcal{O}(10^4)$ above the Standard Model prediction, together with the very low fitted significance, indicates that the residual spectrum is dominated by reactor-correlated background contributions rather than a CEνNS signal. Additional contributions from low-energy excess (LEE) events in the near-threshold region may also be present. To assess the impact of near-threshold events, the fit was repeated using analysis thresholds of 250, 300, and 350 eV. While the resulting 90% CL upper limits show a modest dependence on the threshold choice, the overall conclusion remains unchanged. The fit is influenced by statistical fluctuations across the full analysis region rather than by the lowest-energy bins alone.

Consistent with this interpretation, the reactor–ON-OFF subtracted spectrum for multiple-scatter [Fig. 6(b)] (background-like) events shown in Fig. 12(b) exhibits an exponential-plus-constant behavior. The extracted amplitudes lie in the range $\mathcal{O}(10^4–10^6\ \mathrm{kg}^{-1}\,\mathrm{keV}^{-1}\,\mathrm{day}^{-1})$, confirming the presence of substantial background contributions within the region of interest.

While the reactor–ON-OFF multiple-scatter spectrum is expected to be dominated by reactor-correlated backgrounds, a residual contribution from LEE near threshold cannot be excluded. Such effects are known to be time-dependent, and the reactor-ON and -OFF data were collected during different periods. However, a quantitative assessment of a potential LEE contribution lies beyond the scope of the present work. Additional details on the multiple-scatter event analysis are provided in Appendix B.

V. CONCLUDING REMARKS AND PROSPECTS

The MINER Collaboration successfully installed and operated a cryogenic detection setup near the $\sim$1 $\mathrm{MW_{th}}$ TRIGA research reactor at the Nuclear Science Center (NSC) for a search of coherent elastic neutrino-nucleus scattering (CEνNS). Data were collected during August–September 2022 with exposures of 158 and 381 g-days for reactor-ON and reactor-OFF periods, respectively. The detectors used in this campaign were sapphire (Al_2O_3) crystals, with the primary 72 g detector achieving an excellent baseline energy resolution of (39.99 ± 0.13) eV.

The analysis presented in this work evaluates the sensitivity of the current MINER configuration to CEνNS. The observed detection significance of only 0.01σ indicates no statistically significant CEνNS signal. The best-fit signal strength is found at the physical boundary ($\rho \simeq 0$), and the result is therefore expressed as a 90% CL upper limit of $\rho < 2213$. The observed excess is consistent with residual background contributions. This conclusion is further supported by the simulation results. The data analysis employs rigorous pulse reconstruction and calibration procedures using ^{55}Fe sources, enabling precise energy scale determination across detectors. A signal efficiency correction method, based on template injection into real noise traces has been developed. Systematic uncertainties from all analysis steps, including pulse shape quality cuts, single-scatter selection, and fiducial-volume definition, were carefully evaluated and propagated. These procedures ensure a proper sensitivity estimate despite challenging low-energy backgrounds.

Nevertheless, the low statistical significance suggests that the signal region is dominated by background, which is further supported by the simulation results. Even with enhanced shielding, the current event rate ($\sim$0.14 $\mathrm{kg^{-1}\,day^{-1}}$) remains insufficient to reach competitive sensitivity within a reasonable time frame using the present setup, even after assuming 100% detection efficiency.

To address these limitations and significantly improve sensitivity, the collaboration plans to relocate the experiment to the 85 $\mathrm{MW_{th}}$ High Flux Isotope Reactor (HFIR) at Oak Ridge National Laboratory [44]. The HFIR facility provides a higher $\bar{\nu}_e$ flux, and the MINER setup will be optimized with improved compact shielding and an increased detector payload, featuring multiple primary detectors within the tower.

HFIR is a pressurized, light-water-cooled and -moderated reactor fueled with high-enriched uranium (HEU, 93%

^{235}U), currently operating at 85 MW_{th}. The planned detector deployment will be located approximately 5 m from the reactor core.

Sensitivity projections for MINER at HFIR are shown in Fig. 13. For this study, the nominal background level is assumed to be the same as the current experimentally achieved background rate, corresponding to the present rate of approximately 341 $kg^{-1}\,day^{-1}$. The detector energy threshold is assumed to be 250 eV, consistent with the current analysis. Under these assumptions, a spectral shape analysis is performed using Eq. (4).

The systematic uncertainties taken into account are the 6.77% uncertainty on the background normalization and a 16% systematic uncertainty on the signal modeling. These uncertainties are propagated to estimate the exposure required to achieve a given detection significance, including the corresponding uncertainty band. We find that under the nominal projected background conditions, a 3σ CEνNS detection is expected within approximately 30 kg-days, as shown in Fig. 13(a). Since this represents an optimistic scenario, and the background conditions at the proposed experimental site have not yet been fully characterized, we also study the background rate required to reach a given significance, as shown in Fig. 13(b). In this case, only the 16% systematic uncertainty associated with the signal modeling is included. We find that achieving the same 3σ sensitivity with a reduced exposure of 14 kg-day would require suppressing the background rate to below 150 $kg^{-1}\,day^{-1}$.

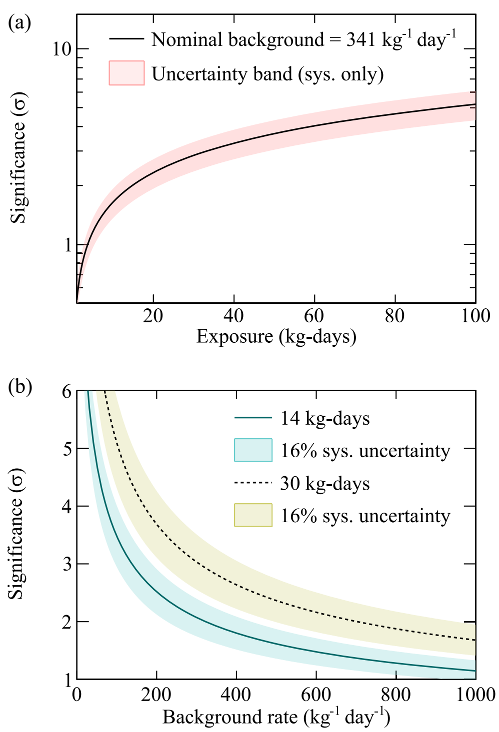

FIG. 13. (a) Projected exposure (kg-day) required at the HFIR site to achieve 3σ and 5σ significance for CEνNS detection, assuming a nominal background rate of $\sim$341 $kg^{-1}\,day^{-1}$. The red shaded band represents the systematic uncertainty around the nominal projection. (b) Background rates required to achieve 3σ and 5σ significance for exposures of 30 and 14 kg-day, respectively. The green and blue shaded bands indicate the 16% systematic uncertainty associated with the SM signal rate estimation.

The full commissioning of the upgraded MINER experiment is planned in the near future and has the potential to significantly improve constraints on CEνNS cross sections and enable precision measurements. The present measurement is limited by reactor-correlated backgrounds and the modest exposure available at the TRIGA facility, resulting in a statistically dominated uncertainty and insufficient sensitivity to the Standard Model CEνNS signal. Nevertheless, it provides an important validation of detector performance, background modeling, and analysis techniques for the future HFIR deployment.

ACKNOWLEDGMENTS

This work was supported by the U.S. Department of Energy (DOE) under Grants No. DE-SC0018981 and No. DE-SC0017859. The authors gratefully acknowledge seed funding from the Mitchell Institute, which enabled early conceptual development and prototyping efforts, as well as the operating costs of this experiment. We acknowledge the support of Texas A&M's Nuclear Science Center management and staff for access to the reactor, associated facilities, and technical support/resources. We also acknowledge the support of the Department of Atomic Energy (DAE) and the Department of Science and Technology (DST), Government of India. This work is partly supported through the J. C. Bose Fellowship of the Anusandhan National Research Foundation (ANRF) awarded to B. M. The work of J. L. N. is supported by the Australian Research Council through the ARC Center of Excellence for Dark Matter Particle Physics, No. CE200100008. The authors thank Mr. Sudipta Das for valuable discussions and his contributions to the signal modeling framework. The authors would like to acknowledge the use of the Kanaad HPC cluster facility at SPS, NISER.

DATA AVAILABILITY

The data that support the findings of this article are not publicly available. The data are available from the authors upon reasonable request.

APPENDIX A: PROFILE-χ^2 ANALYSIS AND 90% CL ESTIMATION

The CEνNS signal-strength parameter, ρ, is determined by minimizing the χ^2 function defined in Eq. (3) using the Minuit package [45]. Since negative CEνNS rates are unphysical, the fit is performed with the constraint $\rho \geq 0$.

The global best-fit point corresponds to the minimum value χ^2_{min}. To determine the upper limit on ρ, a profile-χ^2 scan is performed. For each fixed value of ρ, the nuisance parameters are reminimized and $\Delta\chi^2(\rho) = \chi^2(\rho) - \chi^2_{\mathrm{min}}$ is evaluated. As no statistically significant CEνNS signal is observed, a one-sided upper limit is derived. The 90% confidence-level (CL) upper limit is defined as the value of ρ for which $\Delta\chi^2 = 2.71$, corresponding to a one-sided 90% confidence interval for a single parameter of interest. The upper limit is obtained from the intersection of the profile-χ^2 curve, $\Delta\chi^2(\rho)$, with the $\Delta\chi^2 = 2.71$ criterion, as shown in Fig. 14. The minimum occurs at the physical boundary, $\rho = 0$, indicating no evidence for a CEνNS signal in the present dataset. The profile increases monotonically away from the minimum, and no secondary minima are observed. The resulting 90% CL upper limit estimated in this work is $\rho < 2213$.

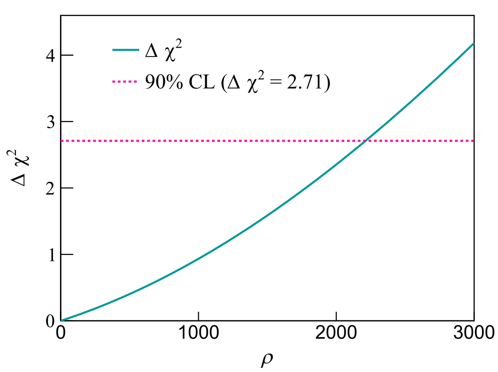

FIG. 14. Profile-χ^2 distribution for the CEνNS normalization parameter ρ obtained from the constrained fit ($\rho \geq 0$). The horizontal pink dashed line corresponds to the one-sided 90% confidence-level criterion, $\Delta\chi^2 = 2.71$. The intersection of the profile with this line defines the reported 90% CL upper limit.

APPENDIX B: MULTIPLE-SCATTERING EVENT SPECTRA

Multiple-scatter events are defined as events that deposit energy in more than one detector, including the primary detector and one or both of the veto detectors.

Figure 15 compares the multiple-scatter energy spectra under reactor-ON and reactor-OFF conditions, with a zoomed-in view of the low-energy region shown in the inset. The presence of the prominent ^{55}Fe peaks in the spectra reflects coincidence activity of the two calibration sources with respect to the position of the detectors. It is not that a single 5.9 keV or 6.5 keV x-ray physically scatters multiple times within the stack. Both the reactor-ON and reactor-OFF spectra exhibit an exponential increase toward lower energies. In addition, a sharp rise is observed near threshold in both datasets. While contributions from low-energy backgrounds are expected, a significant contribution from LEE events cannot be excluded, as they are detector-related effects. A quantitative assessment of the LEE contribution is beyond the scope of the present analysis and will be addressed in a future work.

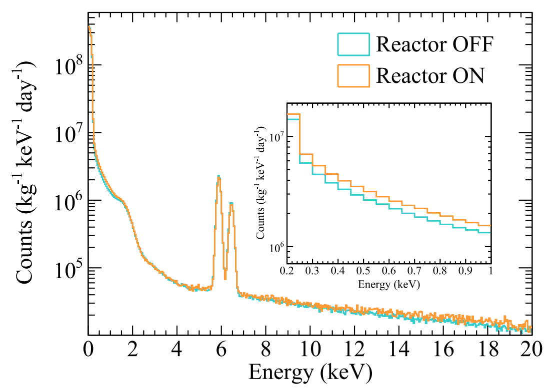

FIG. 15. Multiple-scatter event rate for reactor-ON and -OFF in the range of 0–20 keV. The two peaks correspond to the ^{55}Fe calibration x-ray lines. A more zoomed-in view of the low-energy regions between 200 eV and 1 keV is shown in the inset.

[1] D. Z. Freedman, Coherent effects of a weak neutral current, Phys. Rev. D **9**, 1389 (1974).

[2] A. J. Anderson, J. M. Conrad, E. Figueroa-Feliciano, K. Scholberg, and J. Spitz, Coherent neutrino scattering in dark matter detectors, Phys. Rev. D **84**, 013008 (2011).

[3] M. Atzori Corona, M. Cadeddu, N. Cargioli, F. Dordei, C. Giunti, and G. Masia, Nuclear neutron radius and weak mixing angle measurements from latest COHERENT CsI and atomic parity violation Cs data, Eur. Phys. J. C **83**, 683 (2023).

[4] S. Navas *et al.* (Particle Data Group), Review of particle physics, Phys. Rev. D **110**, 030001 (2024).
[5] D. Akimov *et al.* (COHERENT Collaboration), Observation of coherent elastic neutrino-nucleus scattering, Science **357**, 1123 (2017).
[6] T. S. Kosmas, O. G. Miranda, D. K. Papoulias, M. Tortola, and J. W. F. Valle, Sensitivities to neutrino electromagnetic properties at the TEXONO experiment, Phys. Lett. B **750**, 459 (2015).
[7] P. deNiverville, M. Pospelov, and A. Ritz, Light new physics in coherent neutrino-nucleus scattering experiments, Phys. Rev. D **92**, 095005 (2015).
[8] Beda *et al.*, The results of search for the neutrino magnetic moment in GEMMA experiment, Adv. High Energy Phys. **2012**, 350150 (2012).
[9] J. Papavassiliou, J. Bernabeu, and M. Passera, Neutrino-nuclear coherent scattering and the effective neutrino charge radius, Proc. Sci. HEP2005 (**2006**) 192 [arXiv:hep-ph/0512029].
[10] P. S. Amanik and G. C. McLaughlin, Nuclear neutron form factor from neutrino nucleus coherent elastic scattering, J. Phys. G **36**, 015105 (2009).
[11] S. Kerman, V. Sharma, M. Deniz, H. T. Wong, J. W. Chen, H. B. Li, S. T. Lin, C. P. Liu, and Q. Yue (TEXONO Collaboration), Coherency in neutrino-nucleus elastic scattering, Phys. Rev. D **93**, 113006 (2016).
[12] A. Bernstein, N. Bowden, B. L. Goldblum, P. Huber, I. Jovanovic, and J. Mattingly, Colloquium: Neutrino detectors as tools for nuclear security, Rev. Mod. Phys. **92**, 011003 (2020).
[13] R. Harnik, J. Kopp, and P. A. N. Machado, Exploring ν signals in dark matter detectors, J. Cosmol. Astropart. Phys. 07 (2012) 026.
[14] N. Ackermann *et al.*, Direct observation of coherent elastic antineutrino-nucleus scattering, Nature (London) **643**, 1229 (2025).
[15] S. Karmakar *et al.* (TEXONO Collaboration), New limits on the coherent neutrino-nucleus elastic scattering cross section at the kuo-sheng reactor-neutrino laboratory, Phys. Rev. Lett. **134**, 121802 (2025).
[16] A. Aguilar-Arevalo *et al.* (CONNIE Collaboration), Search for coherent elastic neutrino-nucleus scattering at a nuclear reactor with CONNIE 2019 data, J. High Energy Phys. 05 (2022) 017.
[17] V. Wagner *et al.* (NUCLEUS Collaboration), Exploring CEνNS of reactor neutrinos with the NUCLEUS experiment, J. Phys. Conf. Ser. **2156**, 012118 (2021).
[18] C. Augier *et al.* (Ricochet Collaboration), Fast neutron background characterization of the future Ricochet experiment at the ILL research nuclear reactor, Eur. Phys. J. C **83**, 20 (2023).
[19] A. Armatol *et al.* (Ricochet Collaboration), Characterization of mini-CryoCube detectors from the Ricochet experiment commissioning at the Institut Laue-Langevin, Phys. Rev. D **112**, 112019 (2025).
[20] Alekseev *et al.* (νGeN Collaboration), First results of the νGeN experiment on coherent elastic neutrino-nucleus scattering, Phys. Rev. D **106**, L051101 (2022).
[21] J. B. Dent, B. Dutta, D. Kim, S. Liao, R. Mahapatra, K. Sinha, and A. Thompson, New directions for axion searches via scattering at reactor neutrino experiments, Phys. Rev. Lett. **124**, 211804 (2020).
[22] M. Mirzakhani *et al.*, MINER reactor based search for axionlike particles using sapphire (Al_2O_3) detectors, Phys. Rev. D **112**, 032013 (2025).
[23] A. Aguilar-Arevalo *et al.* (CONNIE Collaboration), Search for light mediators in the low-energy data of the CONNIE reactor neutrino experiment, J. High Energy Phys. 04 (2020) 054.
[24] M. Chaudhuri *et al.*, Development of a large-mass, low-threshold detector system with simultaneous measurements of athermal phonons and scintillation light, Nucl. Instrum. Methods Phys. Res., Sect. A **1053**, 168374 (2023).
[25] S. Verma *et al.*, Low-threshold sapphire detector for rare event searches, Nucl. Instrum. Methods Phys. Res., Sect. A **1046**, 167634 (2023).
[26] K. D. Irwin, S. W. Nam, B. Cabrera, B. Chugg, and B. A. Young, A quasiparticle-trap-assisted transition-edge sensor for phonon-mediated particle detection, Rev. Sci. Instrum. **66**, 5322 (1995).
[27] B. A. Hines, K. M. Sundqvist, D. N. Seitz, and M. E. Huber, Flux-coupled direct feedback in a squid amplifier, IEEE Trans. Appl. Supercond. **21**, 262 (2011).
[28] G. Agnolet *et al.* (MINER Collaboration), Background studies for the MINER coherent neutrino scattering reactor experiment, Nucl. Instrum. Methods Phys. Res., Sect. A **853**, 53 (2017).
[29] S. Maludze, M. Mirzakhani, W. Baker, M. Lee, C. Savage, H. Neog, R. Mahapatra, N. Mirabolfathi, M. Platt, and A. Jastram, Measurement of low energy nuclear recoil events with the phonon-mediated voltage-assisted hybrid detector for rare event searches, Nucl. Instrum. Methods Phys. Res., Sect. A **1070**, 169994 (2025).
[30] B. Anderson and J. Moore, *Optimal Filtering*, Dover Books on Electrical Engineering (Dover Publications, New York, 2012).
[31] C. Fink and S. Watkins, QETpy documentation, Zenodo, 10.5281/zenodo.5903353 (2022).
[32] M. Herman, A. L. Nichols (IAE Agency Collaboration), *Update of X Ray and Gamma Ray Decay Data Standards for Detector Calibration and Other Applications* (International Atomic Energy Agency, 2007).
[33] S. Agostinelli *et al.*, Geant4—A simulation toolkit, Nucl. Instrum. Methods Phys. Res., Sect. A **506**, 250 (2003).
[34] S. Verma, S. Maludze, M. Lee, M. Chaudhuri, V. Iyer, V. K. S. Kashyap, A. Kubik, T. Lin, R. Mahapatra, N. Mirabolfathi, N. Mishra, B. Mohanty, H. Neog, A. Jastram, and M. P. Platta, Large-mass, low-threshold sapphire detector for rare event searches, Nucl. Instrum. Methods Phys. Res., Sect. A **1046**, 167634 (2023).
[35] P. Adari *et al.*, EXCESS workshop: Descriptions of rising low-energy spectra, SciPost Phys. Proc. **9**, 001 (2022).
[36] G. Angloher *et al.*, Latest observations on the low energy excess in CRESST-III, SciPost Phys. Proc. **12**, 013 (2023).
[37] R. K. Romani, Aluminum relaxation as the source of excess low energy events in low threshold calorimeters, J. Appl. Phys. **136**, 124502 (2024).
[38] C. L. Chang *et al.* (TESSERACT Collaboration), Spontaneous generation of athermal phonon bursts within bulk

silicon causing excess noise, low energy background events, and quasiparticle poisoning in superconducting sensors, Appl. Phys. Lett. **127**, 263502 (2025).
[39] V. I. Kopeikin, Flux and spectrum of reactor antineutrinos, Phys. At. Nucl. **75**, 143 (2012).
[40] H. T. Wong *et al.* (TEXONO Collaboration), Search of neutrino magnetic moments with a high-purity germanium detector at the kuo-sheng nuclear power station, Phys. Rev. D **75**, 012001 (2007).
[41] B. Dutta, R. Mahapatra, L. E. Strigari, and J. W. Walker, Sensitivity to *z*-prime and nonstandard neutrino interactions from ultralow threshold neutrino-nucleus coherent scattering, Phys. Rev. D **93**, 013015 (2016).
[42] X. Ji, W. Gu, X. Qian, H. Wei, and C. Zhang, Combined Neyman–Pearson Chi-square: An improved approximation to the poisson-likelihood chi-square, Nucl. Instrum. Methods Phys. Res., Sect. A **961**, 163677 (2020).
[43] M. Gonzalez-Garcia and M. Maltoni, Phenomenology with massive neutrinos, Phys. Rep. **460**, 1 (2008).
[44] D. Chandler, B. R. Betzler, E. E. Davidson, and G. Ilas, Modeling and simulation of a high flux isotope reactor representative core model for updated performance and safety basis assessments, Nucl. Eng. Des. **366**, 110752 (2020).
[45] F. James and M. Roos, Minuit: A system for function minimization and analysis of the parameter errors and correlations, Comput. Phys. Commun. **10**, 343 (1975).